Frontiers of Information Technology & Electronic Engineering
www.jzus.zju.edu.cn; engineering.cae.cn; www.springerlink.com
ISSN 2095-9184 (print); ISSN 2095-9230 (online)
E-mail: jzus@zju.edu.cn

Multiplication extended Kalman filter-aided non-blind star image restoration algorithm based on the heterogeneous blur kernel

Yang LIU‡[1,2,3], Huajian DENG[1], Hao WANG[1,2,3], Zhonghe JIN[1,2,3]

[1]*Micro-Satellite Research Center, Zhejiang University, Hangzhou 310027, China*

[2]*Huanjiang Laboratory, Zhuji 311899, China*

[3]*Key Laboratory of Micro-Nano Satellite Research Zhejiang Province, Hangzhou 310027, China*

E-mail: 12224002@zju.edu.cn; denghuajian@zju.edu.cn; roger@zju.edu.cn; jinzh@zju.edu.cn

Received Mar. 29, 2025; Revision accepted June 10, 2025; Crosschecked Aug. 28, 2025

Abstract: Under dynamic conditions, the smearing effect of star spots on the image plane reduces centroid extraction accuracy, which has an impact on attitude estimation. To enhance the dynamic performance of the star sensor, we propose a multiplication extended Kalman filter (MEKF)-aided non-blind star image restoration algorithm based on the heterogeneous blur kernel. The proposed algorithm consists of three procedures. First, the MEKF is used to estimate the attitude and gyro drift to eliminate the measurement error of the star sensor and gyro drift. Second, the attitude predicted by MEKF is used, which provides initial conditions and accelerates the subsequent algorithm. Finally, a gyro-assisted heterogeneous blur kernel estimation algorithm is presented for restoring non-uniform and nonlinear motion-blurred star images. In contrast to existing dynamic star image deblurring algorithms, which focus mostly on image content, the proposed method emphasizes the cause of motion blur by fusing MEKF and a heterogeneous blur kernel. This leads to significantly enhanced robustness against noise and improved restoration accuracy. Simulation results demonstrate that the proposed method significantly outperforms existing techniques, improving centroid extraction accuracy by up to 59.64% and pointing accuracy across all axes by more than 78.94%.

Key words: Heterogeneous blur kernel estimation; Dynamic conditions; Regional image restoration; Multiplication extended Kalman filter; Gyro drift

https://doi.org/10.1631/FITEE.2500193 **CLC number:** TP391.41; V448.22

1 Introduction

With the advancement of the space industry, there is an increasing demand for attitude measurement, especially under dynamic conditions. The star sensor is one of the most common and important attitude measurement devices, providing high-precision attitude measurement under static conditions. However, under dynamic conditions, star spots will form trails on the image plane. The signal-to-noise ratio (SNR) of star spots will significantly decrease as they spread, and some star spots will become submerged in the noise, resulting in decreased accuracy in centroid extraction and attitude estimation, and in some cases, identification failure. To enhance the dynamic performance of star sensors, Ma et al. (2025) recommended restoring these star streaks.

Blind and non-blind restoration algorithms for star image restoration algorithms can be categorized according to whether external angular velocity or angular acceleration information can be obtained. In addition, with the rapid development of neural networks, an increasing number of deep learning-based image restoration algorithms have been proposed.

‡ Corresponding author
ORCID: Yang LIU, https://orcid.org/0009-0008-9253-2683
© Zhejiang University Press 2025

However, there is still a significant gap between these methods and their practical deployment in star sensor systems (Wang H et al., 2020).

Blind restoration algorithms estimate blur parameters exclusively from a single-frame star image without angular velocity information (Sun et al., 2013; Jiang et al., 2017; Hou et al., 2021; Yang et al., 2025). Although these approaches are convenient and straightforward to implement, their estimation accuracy is significantly lower than that of non-blind restoration methods.

In the non-blind methods, blur kernel can be obtained by angular velocity and acceleration using external devices (Fei et al., 2012; Sun et al., 2014b; Wang KD et al., 2014; Wang SQ et al., 2018). However, these algorithms have dual limitations. First, they overlook the error caused by gyro drift, disregarding the impact of gyro drift on the overall accuracy of the restoration process. Sun et al. (2014a) used the extended Kalman filter (EKF) to estimate the position of individual star spots and gyro drift under dynamic conditions. However, their method suffers from increasing computational redundancy as the number of star points increases, because each star must be processed separately. Second, these methods rely on preliminary angular velocity assumptions, estimating the star spot's trailing path based on prior angular velocity, and interpreting motion blur in star images in a linear manner to calculate the blur kernel. For example, Yi et al. (2023) assumed that the angular velocity is perpendicular to the Z axis of the star sensor, so the star spots form straight lines on the image plane, and then the linear blur kernels are calculated according to the trajectories. Ma et al. (2016) established a proportional relationship between the rotation angle perpendicular to the Z axis and the field of view. This relationship was used to estimate the linear blur kernel. Zhang et al. (2012) hypothesized that the star sensor undergoes rotation around the Z axis, causing star spots to form arcs on the image plane. Then the blur kernel was calculated according to the corresponding chord. However, these priors and linear explanation cannot fully capture the non-uniform and nonlinear nature of the motion blur presented in star images (Spiller and Curti, 2022). Therefore, addressing these shortcomings is crucial for enhancing the robustness and precision of the star image restoration algorithm.

Inspired by Sun et al. (2014a), we propose a multiplication extended Kalman filter (MEKF)-aided non-blind star image restoration algorithm based on a heterogeneous blur kernel to address the two aforementioned challenges, assuming a one-to-one correspondence between the spacecraft attitude and the star spot positions on the image plane. MEKF is one of the most widely used attitude estimation methods in the aerospace field (Lefferts et al., 1982; Markley, 2003; Sola, 2017; Tian et al., 2025). MEKF has the advantage of not only suppressing the gyro drift error but also allowing its predicted attitude to be used to determine star spot positions, providing the initial conditions for the subsequent heterogeneous blur kernel estimation. To address non-uniform and nonlinear motion blur in star images, the proposed algorithm emphasizes that eliminating pixel-by-pixel motion blur is the key to image restoration. Therefore, a heterogeneous blur kernel is presented. In this algorithm, the traditional blur kernel is replaced by a set of diverse blur kernels, each tailored to the characteristics of a single pixel within the star positions. The pixel blur kernel is determined using its specific position and motion, which means that the calculation of the blur kernel no longer requires estimating the star spot's trailing path based on a prior angular velocity. This allows the algorithm to focus on understanding the root cause of the blur rather than relying solely on the image content. Such an innovative strategy enhances the adaptability of the restoration process and can more accurately deal with the complex motion blur existing in star images, making the strategy suitable for image restoration in various situations.

2 State optimization estimation based on MEKF

After years of development, MEKF not only has a sound theory, but also has been verified by several rigorous experiments, and thus plays an important role in attitude estimation. At present, it is widely used in the fields of robotics, navigation, and sensor fusion. There are various kinds of attitude expressions, the quaternion being the most common due to its non-singularity and low dimension. However, although the quaternion has four terms, it has only three real degrees of freedom; one of these terms is limited by the other three terms and the norm of the quaternion. It signifies that the covariance matrix of

the quaternion is theoretically singular, causing some difficulties for numerical calculations. To solve this problem, a modified Rodrigues parameter (MRP) $\boldsymbol{a}$ is used to describe attitude in this paper:

$$\frac{1}{4}\boldsymbol{a}=\frac{\underline{\boldsymbol{q}}}{1+q_4}=\boldsymbol{e}\tan\frac{\theta}{4}, \tag{1}$$

where $\boldsymbol{q}=\begin{bmatrix}\underline{\boldsymbol{q}}\\ q_4\end{bmatrix}=[q_1\ q_2\ q_3\ q_4]^{\mathrm{T}}$ denotes the attitude quaternion, and $\underline{\boldsymbol{q}}$ and q_4 denote the vector and scalar parts of the quaternion, respectively. $\boldsymbol{e}$ and θ represent the corresponding rotation axis and angle of the quaternion, respectively. The coefficient term is to ensure that $||\boldsymbol{a}||\approx\theta$ for small rotations.

As shown in Eq. (1), MRP is an unconstrained three-dimensional vector with the same number of parameters as degrees of freedom, avoiding the problem of over-parameterization. The singularities occur at $\theta=\pm2\pi$, while MEKF always operates close to the origin. Thus, singularity is no longer a problem (Madyastha et al., 2011; Zamani et al., 2015).

Before proceeding with the derivation of the subsequent content, Table 1 describes some of the variables used in this paper.

Table 1 Definitions of some variables

Variable	Description
$\boldsymbol{\omega}$	True value
$\tilde{\boldsymbol{\omega}}$	Estimate
$\hat{\boldsymbol{\omega}}$	Measured value

2.1 Prediction

Attitude error MRP $\delta\boldsymbol{a}$ and gyro drift $\boldsymbol{b}$ are selected as the state vector $\boldsymbol{x}$:

$$\boldsymbol{x}=[\delta\boldsymbol{a}\ \boldsymbol{b}]^{\mathrm{T}}. \tag{2}$$

A widely used model of the gyro is given as follows:

$$\begin{cases}\boldsymbol{\omega}=\boldsymbol{A}_{\mathrm{bg}}(\hat{\boldsymbol{\omega}}_{\mathrm{g}}-\boldsymbol{b}-\boldsymbol{\eta}_{\mathrm{g}}),\\ \dot{\boldsymbol{b}}=\boldsymbol{\eta}_{\mathrm{r}},\end{cases} \tag{3}$$

where $\boldsymbol{\omega}$ and $\hat{\boldsymbol{\omega}}_{\mathrm{g}}$ denote the true and measured angular velocity, respectively. $\boldsymbol{\eta}_{\mathrm{g}}$ and $\boldsymbol{\eta}_{\mathrm{r}}$ denote the white noise for gyro, regarded as angle random walk (ARW) and rate random walk (RRM), respectively. To facilitate the subsequent derivation, the gyro coordinate system is assumed to be consistent with the body coordinate system of the satellite, that is, $\boldsymbol{A}_{\mathrm{bg}}=\boldsymbol{I}_{3\times3}$.

The estimated gyro angular velocity $\tilde{\boldsymbol{\omega}}_{\mathrm{g}}$ is described as

$$\tilde{\boldsymbol{\omega}}_{\mathrm{g}}=\boldsymbol{\omega}_{\mathrm{g}}-\tilde{\boldsymbol{b}}, \tag{4}$$

where $\boldsymbol{\omega}_{\mathrm{g}}$ and $\tilde{\boldsymbol{b}}$ denote the true angular velocity and estimated drift of the gyro, respectively.

Letting $\otimes$ denotes the multiplication of quaternions, the error quaternion and quaternion differential equation are shown in Eqs. (5) and (6), respectively:

$$\tilde{\boldsymbol{q}}=\boldsymbol{q}\otimes\delta\boldsymbol{q}, \tag{5}$$

$$\dot{\boldsymbol{q}}=\frac{1}{2}\boldsymbol{q}\otimes\begin{bmatrix}\boldsymbol{\omega}\\ \boldsymbol{0}\end{bmatrix}, \tag{6}$$

where $\tilde{\boldsymbol{q}}$ and $\boldsymbol{q}$ denote the estimated and true quaternions, respectively. $\delta\boldsymbol{q}$ denotes the error quaternion, which can be obtained by integrating the angular velocity.

Differentiate both sides of Eqs. (5) and (6) so that we can obtain

$$\dot{\delta\boldsymbol{q}}=\frac{1}{2}\delta\boldsymbol{q}\otimes\begin{bmatrix}\tilde{\boldsymbol{\omega}}\\ \boldsymbol{0}\end{bmatrix}-\frac{1}{2}\begin{bmatrix}\boldsymbol{\omega}\\ \boldsymbol{0}\end{bmatrix}\otimes\delta\boldsymbol{q}. \tag{7}$$

Then, Eqs. (1) and (7) are combined to obtain the partial derivative of the attitude error $\delta\boldsymbol{a}$ with respect to time:

$$\begin{aligned}\dot{\delta\boldsymbol{a}}=&\left(\left(1-\frac{(\delta\boldsymbol{a})^{\mathrm{T}}\delta\boldsymbol{a}}{16}\right)\boldsymbol{I}_{3\times3}+\frac{\delta\boldsymbol{a}(\delta\boldsymbol{a})^{\mathrm{T}}}{8}\right)(\tilde{\boldsymbol{\omega}}-\boldsymbol{\omega})\\&-\frac{1}{2}[(\tilde{\boldsymbol{\omega}}+\boldsymbol{\omega})\times]\delta\boldsymbol{a},\end{aligned} \tag{8}$$

where $[\boldsymbol{\omega}\times]$ is the following matrix:

$$[\boldsymbol{\omega}\times]=\begin{bmatrix}0&-\omega_z&\omega_y\\ \omega_z&0&-\omega_x\\ -\omega_y&\omega_x&0\end{bmatrix}. \tag{9}$$

The state transition equations can be described as

$$\dot{\boldsymbol{x}}(t)=f(\boldsymbol{x}(t))+\boldsymbol{w}(t), \tag{10}$$

where $\boldsymbol{w}(t)$ denotes the process noise, which is assumed to be zero-mean Gaussian noise with covariance $\boldsymbol{Q}$. $f(\cdot)$ is the system state transition function.

The expression of the state transition equation in the discrete case is as follows:

$$\begin{aligned}\tilde{\boldsymbol{x}}_{k+1}^{-}&=\tilde{\boldsymbol{x}}_k^{+}+\frac{\partial\boldsymbol{x}}{\partial t}|_{\boldsymbol{x}=\tilde{\boldsymbol{x}}_k^{+}}\delta t+\frac{1}{2}\frac{\partial^2\boldsymbol{x}}{\partial t^2}|_{\boldsymbol{x}=\tilde{\boldsymbol{x}}_k^{+}}\delta t^2\\&=\tilde{\boldsymbol{x}}_k^{+}+\boldsymbol{f}_k\delta t+\frac{1}{2}\boldsymbol{A}_k\boldsymbol{f}_k\delta t^2,\end{aligned} \tag{11}$$

where $\tilde{\boldsymbol{x}}_k^+$ is

$$\tilde{\boldsymbol{x}}_k^+ = \begin{bmatrix} \delta\tilde{\boldsymbol{a}}_k \\ \tilde{\boldsymbol{b}}_k^+ \end{bmatrix}. \tag{12}$$

Here, superscript "−" denotes prior state estimates, and "+" denotes posterior state estimates.

The attitude error $\delta\tilde{\boldsymbol{a}}_k$ between step k and $k+1$ can be approximated by multiplying the attitude error of the gyro sampling interval:

$$q(\delta\tilde{\boldsymbol{a}}_k) = \delta\boldsymbol{q}_{\mathrm{g},1} \otimes \delta\boldsymbol{q}_{\mathrm{g},2} \otimes ... \otimes \delta\boldsymbol{q}_{\mathrm{g},n}, \tag{13}$$

where $\delta\boldsymbol{q}_{\mathrm{g},i}$ is the error quaternion between gyro sampling intervals δt_{g} between steps k and $k+1$.

$$\delta\boldsymbol{q}_{\mathrm{g}} = \begin{bmatrix} \bar{\tilde{\boldsymbol{\omega}}}_{\mathrm{g}}\delta t_{\mathrm{g}} \\ 1 \end{bmatrix}. \tag{14}$$

$\boldsymbol{f}_k$ can be obtained from Eqs. (3) and (8):

$$\boldsymbol{f}_k = \frac{\partial \boldsymbol{x}}{\partial t}|_{\boldsymbol{x}=\tilde{\boldsymbol{x}}_k^+} = \begin{bmatrix} \dot{\delta\boldsymbol{a}} \\ \dot{\boldsymbol{b}} \end{bmatrix}. \tag{15}$$

$\boldsymbol{A}_k$ is a Jacobian matrix:

$$\begin{aligned} \boldsymbol{A}_k = \left.\frac{\partial \boldsymbol{f}}{\partial \boldsymbol{x}}\right|_{\boldsymbol{x}=\tilde{\boldsymbol{x}}_k^+} &= \left.\begin{bmatrix} \frac{\partial \dot{\delta\boldsymbol{a}}}{\partial \delta\boldsymbol{a}} & \frac{\partial \dot{\delta\boldsymbol{a}}}{\partial \boldsymbol{b}} \\ \frac{\partial \dot{\boldsymbol{\eta}}_{\mathrm{r}}}{\partial \delta\boldsymbol{a}} & \frac{\partial \dot{\boldsymbol{\eta}}_{\mathrm{r}}}{\partial \boldsymbol{b}} \end{bmatrix}\right|_{\boldsymbol{x}=\tilde{\boldsymbol{x}}_k^+} \\ &= \begin{bmatrix} \boldsymbol{F}_{\boldsymbol{a}} & \boldsymbol{F}_{\boldsymbol{b}} \\ \boldsymbol{0}_{3\times3} & \boldsymbol{0}_{3\times3} \end{bmatrix}, \end{aligned} \tag{16}$$

where $\boldsymbol{F}_{\boldsymbol{a}}$ and $\boldsymbol{F}_{\boldsymbol{b}}$ are

$$\begin{aligned} \boldsymbol{F}_{\boldsymbol{a}} =& \frac{1}{8}\left((\delta\boldsymbol{a})^{\mathrm{T}}\delta\boldsymbol{\omega}\boldsymbol{I}_{3\times3} + \delta\boldsymbol{a}(\delta\boldsymbol{\omega})^{\mathrm{T}} - \delta\boldsymbol{\omega}(\delta\boldsymbol{a})^{\mathrm{T}}\right) \\ & - \frac{1}{2}[(\tilde{\boldsymbol{\omega}} + \boldsymbol{\omega})\times], \end{aligned} \tag{17}$$

$$\boldsymbol{F}_{\boldsymbol{b}} = \left(1 - \frac{(\delta\boldsymbol{a})^{\mathrm{T}}\delta\boldsymbol{a}}{16}\right)\boldsymbol{I}_{3\times3} + \frac{\delta\boldsymbol{a}(\delta\boldsymbol{a})^{\mathrm{T}}}{8} - \frac{1}{2}[\delta\boldsymbol{a}\times], \tag{18}$$

and $\delta\boldsymbol{\omega}$ can be calculated from Eqs. (3) and (4):

$$\delta\boldsymbol{\omega} = \tilde{\boldsymbol{\omega}} - \boldsymbol{\omega} = \boldsymbol{b} - \tilde{\boldsymbol{b}} + \boldsymbol{\eta}_{\mathrm{g}}. \tag{19}$$

The predicted error covariance matrix $\boldsymbol{P}$ satisfies Eq. (20):

$$\boldsymbol{P}_{k+1}^- = \boldsymbol{\phi}_k\boldsymbol{P}_k^+\boldsymbol{\phi}_k^{\mathrm{T}} + \boldsymbol{G}_k\boldsymbol{Q}_k\boldsymbol{G}_k^{\mathrm{T}}, \tag{20}$$

where $\boldsymbol{\phi}_k$ is

$$\boldsymbol{\phi}_k = \boldsymbol{I}_{6\times6} + \boldsymbol{A}_k\delta t. \tag{21}$$

$\boldsymbol{G}_k$ is calculated by

$$\boldsymbol{G}_k = \begin{bmatrix} \frac{\partial \dot{\delta\boldsymbol{a}}}{\partial \boldsymbol{\eta}_{\mathrm{g}}} & \frac{\partial \dot{\delta\boldsymbol{a}}}{\partial \boldsymbol{\eta}_{\mathrm{r}}} \\ \frac{\partial \dot{\boldsymbol{\eta}}_{\mathrm{r}}}{\partial \boldsymbol{\eta}_{\mathrm{g}}} & \frac{\partial \dot{\boldsymbol{\eta}}_{\mathrm{r}}}{\partial \boldsymbol{\eta}_{\mathrm{r}}} \end{bmatrix} = \begin{bmatrix} \boldsymbol{F}_{\boldsymbol{b}} & \boldsymbol{0}_{3\times3} \\ \boldsymbol{0}_{3\times3} & \boldsymbol{I}_{3\times3} \end{bmatrix}, \tag{22}$$

and $\boldsymbol{Q}$ can be obtained by

$$\boldsymbol{Q}_k = E\left[\begin{bmatrix} \boldsymbol{\eta}_{\mathrm{g}} \\ \boldsymbol{\eta}_{\mathrm{r}} \end{bmatrix}\begin{bmatrix} \boldsymbol{\eta}_{\mathrm{g}} \\ \boldsymbol{\eta}_{\mathrm{r}} \end{bmatrix}^{\mathrm{T}}\right], \tag{23}$$

where E is the expectation calculation.

2.2 Improved update

The attitude $\boldsymbol{z}$ measured by the star sensor is used as the measurement vector, and the attitude measurement equation is

$$\boldsymbol{z}(t) = \boldsymbol{q}(\boldsymbol{a}(t)) \otimes \boldsymbol{q}(\delta\boldsymbol{a}(t)), \tag{24}$$

where $\boldsymbol{a}(t)$ denotes the true attitude and $\delta\boldsymbol{a}(t)$ denotes zero-mean Gaussian measurement error with variance $\boldsymbol{R}$.

The state vector is updated as follows:

$$\begin{aligned} \boldsymbol{H}_{k+1} &= [\boldsymbol{I}_{3\times3}\ \boldsymbol{0}_{3\times3}], \\ \boldsymbol{S}_{k+1} &= \boldsymbol{H}_{k+1}\boldsymbol{P}_{k+1}^-\boldsymbol{H}_{k+1}^{\mathrm{T}} + \boldsymbol{R}_{k+1}, \\ \boldsymbol{K}_{k+1} &= \boldsymbol{P}_{k+1}^-\boldsymbol{H}_{k+1}^{\mathrm{T}}\boldsymbol{S}_{k+1}^{-1}, \end{aligned} \tag{25}$$

$$\delta\boldsymbol{x}_{k+1}^+ = \begin{bmatrix} \delta\boldsymbol{a}_{k+1}^+ \\ \delta\boldsymbol{b}_{k+1}^+ \end{bmatrix} = \boldsymbol{K}_{k+1}(\boldsymbol{q}^{-1}(\tilde{\boldsymbol{a}}_{k+1}^-) \otimes \boldsymbol{z}_{k+1}), \tag{26}$$

$$\boldsymbol{P}_{k+1}^{\mathrm{pred}} = (\boldsymbol{I}_{6\times6} - \boldsymbol{K}_{k+1}\boldsymbol{H}_{k+1})\boldsymbol{P}_{k+1}^-, \tag{27}$$

where $\tilde{\boldsymbol{a}}_{k+1}^-$ denotes the prediction attitude:

$$\boldsymbol{q}(\tilde{\boldsymbol{a}}_{k+1}^-) = \boldsymbol{q}(\tilde{\boldsymbol{a}}_k^+) \otimes \boldsymbol{q}(\delta\tilde{\boldsymbol{a}}_{k+1}^-). \tag{28}$$

The updated state error is transferred to the attitude and reset to Eq. (29):

$$\begin{cases} \boldsymbol{q}(\tilde{\boldsymbol{a}}_{k+1}^+) = \boldsymbol{q}(\tilde{\boldsymbol{a}}_{k+1}^-) \otimes \boldsymbol{q}(\delta\boldsymbol{a}_{k+1}^+), \\ \tilde{\boldsymbol{b}}_{k+1}^+ = \tilde{\boldsymbol{b}}_{k+1}^- + \delta\boldsymbol{b}_{k+1}^+, \\ \boldsymbol{P}_{k+1}^+ = \boldsymbol{J}_{k+1}\boldsymbol{P}_{k+1}^{\mathrm{pred}}\boldsymbol{J}_{k+1}^{\mathrm{T}}, \end{cases} \tag{29}$$

where $\boldsymbol{J}_{k+1}$ is

$$\boldsymbol{J}_{k+1} = \boldsymbol{I}_{3\times3} - \frac{1}{2}[\delta\boldsymbol{a}_{k+1}^+\times]. \tag{30}$$

The detailed flow of the proposed MEKF is shown in Fig. 1.

3 Star image restoration

Table 2 lists some key parameters of the star sensor used in this paper. Subsequent discussions are based on these parameters.

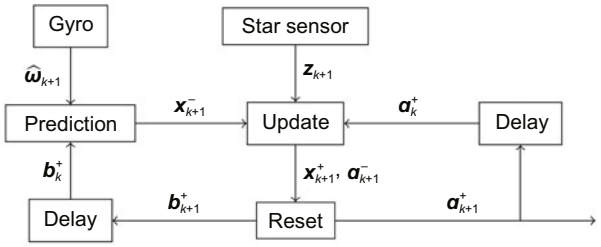

Fig. 1 Flow of the MEKF. $\hat{w}_{k+1}$ is the angular velocity measured by a gyroscope

Table 2 Parameters of the star sensor

Parameter	Unit	Typical value
Entrance pupil diameter	mm	25
Focal length	mm	25
Limiting magnitude		6
Exposure time	ms	80
Resolution	pixels	1024×1280
Pixel size	μm	5.3
Field of view	°	12.5

As mentioned above, in the case of motion, the smearing effect reduces the accuracy of centroid extraction, resulting in decreased identification accuracy and success rates. Therefore, the motion-blurred image should be restored to improve the accuracy of centroid extraction.

3.1 Heterogeneous motion blur model

It is well known that the angular velocity of a star sensor typically possesses three-axis components. Furthermore, the trajectory of a star spot on the image plane is a segment of a conic curve, indicating that the motion blur in the star image is both non-uniform and nonlinear. If a uniform or linear blur kernel is still used for star image restoration, the efficacy of the restoration process is compromised, resulting in reduced accuracy in centroid extraction. Therefore, a heterogeneous motion blur model is established to deal with non-uniform and nonlinear-blurred image restoration, in which the cause of motion blur of each pixel is considered rather than the content of the star image.

Letting $*$ as the general convolution operator, the image degradation model can be expressed as

$$g = h * f_{\mathrm{i}} + \eta, \tag{31}$$

where g and f_{i} denote the images before and after degradation, respectively. h denotes the heterogeneous blur kernel map, with a different blur kernel for each pixel in f_{i}. η denotes the additive noise. Regardless of the additive noise, at each pixel of g, there is

$$g(i,j) = \sum_{i',j'} h_{i',j'}(i,j) f_{\mathrm{i}}(i+i', j+j'), \tag{32}$$

where $h_{i',j'}(i,j)$ denotes the blur kernel that operates on the pixel $(i+i', j+j')$ around the pixel (i,j). The blur kernel estimation is the most important aspect of image restoration. According to Eq. (32), the heterogeneous blur kernel consists of a series of blur kernels that are related to the position and motion of pixels (Gong et al., 2017). As shown in Fig. 2,

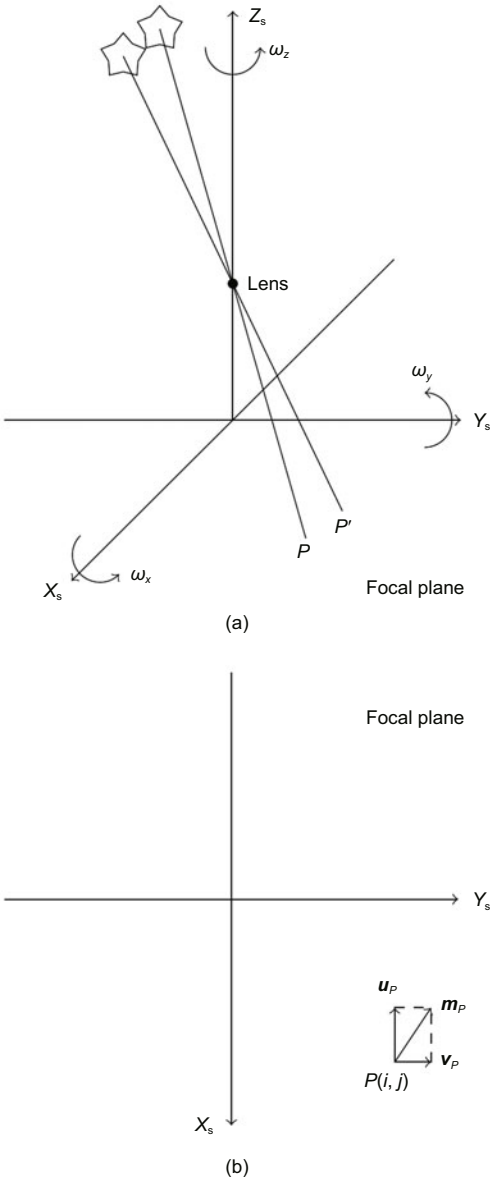

Fig. 2 Position and blur kernel of the star spot: (a) imaging model of the star sensor; (b) blur kernel on a single pixel

the motion of a pixel P located at (i,j) during the imaging process can be represented by a linear two-dimensional motion vector $(\boldsymbol{u}_P,\boldsymbol{v}_P)$, where $\boldsymbol{u}_P$ and $\boldsymbol{v}_P$ represent the motion in the X- and Y-axis directions, respectively.

Letting (x_0,y_0) be the intersection point of the main optical axis and the image plane of the star sensor and f_l be the focal length, the two-dimensional motion vector $(\boldsymbol{u}_P,\boldsymbol{v}_P)$ corresponding to pixel P can be expressed as

$$\begin{cases} ||\boldsymbol{u}_P|| = (-\bar{\omega}_z(j-y_0)-\bar{\omega}_y f_\mathrm{l})\delta t, \\ ||\boldsymbol{v}_P|| = (\bar{\omega}_z(i-x_0)+\bar{\omega}_x f_\mathrm{l})\delta t, \end{cases} \tag{33}$$

where $\bar{\boldsymbol{\omega}}=[\bar{\omega}_x,\bar{\omega}_y,\bar{\omega}_z]^\mathrm{T}$ is the average angular velocity after compensating for the drift over the exposure time δt.

Then the blur kernel on P is expressed as

$$h_{i',j'}(P)=\begin{cases} 0, & ||(i',j')||_2 \geq \dfrac{||\boldsymbol{m}_P||_2}{2}, \\ \dfrac{1}{||\boldsymbol{m}_P||_2}\delta(\boldsymbol{u}_P j'-\boldsymbol{v}_P i'), & \text{otherwise}, \end{cases} \tag{34}$$

$$||\boldsymbol{m}_P||_2 = ||(\boldsymbol{u}_P,\boldsymbol{v}_P)||_2. \tag{35}$$

Although the proposed algorithm assumes that the blur kernel on a single pixel is linear, it makes no assumptions about the motion blur of the image, making the method suitable for various scenes and able to deal with various motion blurs.

3.2 Estimation of star position and blur kernel

With MEKF, the predicted attitude $\boldsymbol{q}$ can be obtained. Assuming that the coordinate system of the star sensor is aligned with that of the satellite, and that the main optical axis of the star sensor under the satellite coordinate system is denoted as $\boldsymbol{Z}_0$, then the optical axis direction $\boldsymbol{Z}$ under the inertial frame can be calculated by Eq. (36):

$$\begin{bmatrix}\boldsymbol{Z}\\ \boldsymbol{0}\end{bmatrix} = \boldsymbol{q}\otimes\begin{bmatrix}\boldsymbol{Z}_0\\ \boldsymbol{0}\end{bmatrix}\otimes\boldsymbol{q}^{-1}. \tag{36}$$

The angle between the star vector in the navigation star catalog and the optical axis in the inertial frame is calculated. Star vectors with angles less than half the field of view are converted to the sensor coordinate system and projected onto the image plane. The projection positions correspond to the star positions at the center of the exposure time.

Assuming that the vector of the star spot in the field of view is $\boldsymbol{v}$ under the reference frame and $\boldsymbol{w}$ under the sensor frame, and that the attitude quaternion is $\boldsymbol{q}$, the vector transformations can be expressed as Eq. (37):

$$\begin{bmatrix}\boldsymbol{w}\\ \boldsymbol{0}\end{bmatrix}=\boldsymbol{q}^{-1}\otimes\begin{bmatrix}\boldsymbol{v}\\ \boldsymbol{0}\end{bmatrix}\otimes\boldsymbol{q}=\frac{(x-x_0,y-y_0,-f)^\mathrm{T}}{\sqrt{(x-x_0)^2+(y-y_0)^2+f^2}}, \tag{37}$$

where (x_0,y_0) is the intersection of the main optical axis and the image plane, f_l is the focal length of the star sensor, and (x,y) is the center of the star's projection on the image plane. These parameters are measured in pixels to reduce the complexity of the calculation.

The update rate of the gyro is usually hundreds of Hertz; therefore, the angular velocity is considered as a constant between the adjacent sampling intervals of the gyro, and the corresponding error quaternion during the time interval from time t to $t+\delta t$ ($\delta\boldsymbol{q}_t^{t+\delta t}$) can be calculated according to Eq. (14).

By combining Eqs. (14) and (37), the estimate of the star vector $\boldsymbol{w}_{t+\delta t}$ at time $t+\delta t$ can be obtained:

$$\begin{bmatrix}\boldsymbol{w}_{t+\delta t}\\ \boldsymbol{0}\end{bmatrix}=(\delta\boldsymbol{q}_t^{t+\delta t})^{-1}\otimes\begin{bmatrix}\boldsymbol{w}_t\\ \boldsymbol{0}\end{bmatrix}\otimes\delta\boldsymbol{q}_t^{t+\delta t}. \tag{38}$$

The star position at time $t+\delta t$ can be obtained by

$$\begin{cases} \boldsymbol{x}_{t+\delta t} = -\dfrac{\boldsymbol{w}_{t+\delta t,x}}{\boldsymbol{w}_{t+\delta t,z}}f_\mathrm{l}+x_0, \\ \boldsymbol{y}_{t+\delta t} = -\dfrac{\boldsymbol{w}_{t+\delta t,y}}{\boldsymbol{w}_{t+\delta t,z}}f_\mathrm{l}+y_0. \end{cases} \tag{39}$$

Similarly, the star position at time $t-\delta t$ can also be derived. Then the star position (x_i,y_i) corresponding to each gyro sampling during the entire exposure time is obtained. According to these positions, the motion trajectory of the star spot on the image plane can be obtained, and the region within four pixels of the trajectory is taken as the star position. The heterogeneous blur kernel of the star position is calculated by Eqs. (33) and (34).

3.3 Regional image restoration

As seen from Eq. (31), even if the blur kernel is obtained, the presence of additive noise makes it difficult to obtain a deblurred image by deconvolution. At present, the pre-processing of dynamic star images is relatively mature, and Gaussian correlation filter and top-hat transformation are used for

denoising (Bright and Steel, 1987; Sun et al., 2013). Next, the process of regional image restoration is introduced.

To accelerate the algorithm, image restoration is performed only in the star position. According to Bayes' theorem and Eq. (32), image restoration that eliminates image noise can be expressed as an iterative process:

$$\begin{cases} f_{\mathrm{i}}^{r+1}(i) = f_{\mathrm{i}}^{r}(i) \sum\limits_{k} \dfrac{h_i(k) g(k)}{\sum\limits_{j} h_j(k) f_{\mathrm{i}}^{r}(j)}, \\ f_{\mathrm{i}}^{1}(i) = \sum\limits_{k} \dfrac{h_i(k) g(k)}{\sum\limits_{j} h_j(k)}, \end{cases} \tag{40}$$

where r represents the number of iterations, and i, j, and k represent the indices of pixels.

The whole process of star image restoration is introduced on this basis, as shown in Fig. 3.

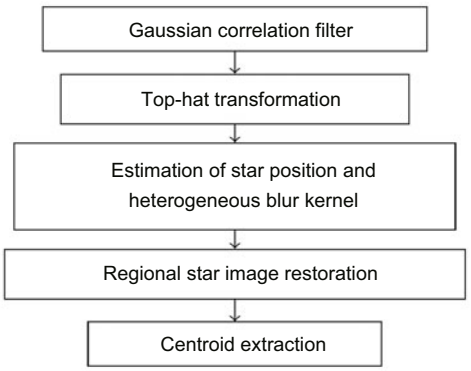

Fig. 3 Flow of dynamic star image restoration

4 Simulations and results

To confirm the effectiveness of the proposed algorithm, a mathematical simulation model with adjustable parameters is established based on Simulink and a micro-satellite orbiting at an altitude of 490 km. The model is shown in Fig. 4. In the simulations, the inputs of the model are the initial attitude, angular velocity, and orbit time, and the output is the real attitude determined by the attitude dynamics module and sensor measurement data. The update rates of the star sensor and the gyro of the micro-satellite are 5 and 100 Hz, respectively. The simulations are divided into the following parts:

1. Estimation of the star position and blur kernel is closely related to MEKF performance. Therefore, the attitude and gyro drift estimation accuracy of the MEKF are tested under different angular velocities.

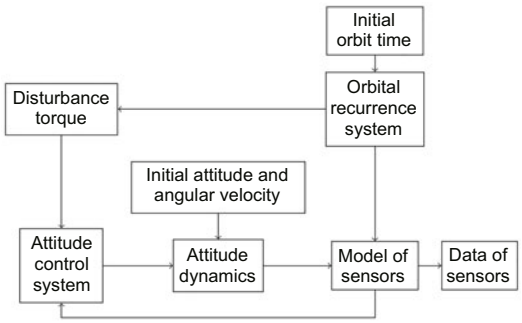

Fig. 4 Simulation model

2. To validate the restoration performance of the algorithm on nonlinear motion-blurred images of varying degrees, the performance of the proposed algorithm is compared with those of two other linear blur kernel estimation algorithms on the nonlinear-blurred star images with different proportions of Z-axis components of angular velocities.

3. To assess the suitability and effectiveness of the proposed algorithm, the restoration effects of the proposed algorithm and the other two algorithms on the blurred images with different angular velocities are compared. In addition, the proposed algorithm with an uncompensated measurement error of the star sensor and gyro drift is used as a comparison to evaluate the improvement of MEKF in image restoration. Furthermore, the attitude estimation accuracy of the star image recovered by the proposed algorithm is tested.

The simulated motion-blurred star image is generated as follows (Li et al., 2013): First, a preset angular velocity is input into the attitude dynamics module of the satellite simulation model to generate the corresponding attitude, the measured angular velocity, and the measured attitude quaternion. The measurement errors are shown in Table 3. Measurements from the gyro and star sensor are used for MEKF to estimate drift and attitude. Second, a series of continuous simulated static star images is generated according to the unbiased attitude, and then the static star images are blurred according to the preset angular velocity during the exposure time. Finally, the simulated motion-blurred star images are obtained by adding Gaussian noise. One of the simulated motion-blurred star images is shown in Fig. 5.

Table 3 Fixed noise

Variable		Unit	Value
$\delta\boldsymbol{\theta}$	X	arcsec	30
	Y		30
	Z		200
$\boldsymbol{b}$	X	(°)/s	0.20
	Y		0.50
	Z		0.10
$\boldsymbol{\eta}_{\mathrm{g}}$		(°)/$\sqrt{\mathrm{h}}$	0.15
$\boldsymbol{\eta}_{\mathrm{r}}$		(°)/(h·$\sqrt{\mathrm{h}}$)	1.00

Fig. 5 Simulated motion-blurred star image

4.1 The performance of MEKF

In the simulations, the inertial frame is selected as the reference frame and the initial attitude quaternion of the satellite is $[0\ 0\ 0\ 1]^{\mathrm{T}}$. The measurement models of the star sensor and gyro are Eqs. (5) and (3), respectively. The fixed noise is shown in Table 3. The angular velocity is set in an arbitrary direction, increasing from 5 to 10 (°)/s with a step size of 0.1 (°)/s. The index of attitude estimation accuracy is the root mean square error (RMSE) of the three-axis error angle after convergence of MEKF, and the error angle is given by Eq. (1). The index of gyro drift estimation accuracy is the RMSE of the difference between the estimated value and the true value after the convergence of MEKF.

Fig. 6 shows the estimation errors of the attitude and gyro drift at an angular velocity of 5 (°)/s, and Fig. 7 shows the details of the estimation errors for the attitude and gyro drift after the MEKF convergence between 200 and 1000 s. It can be seen that MEKF converges quickly and can effectively suppress the measurement error of the star sensor and accurately estimate the gyro drift. The estimation accuracies of attitude and gyro drift are shown in Fig. 8. The three-axis estimation accuracies of attitude and gyro drift are about $[22.38, 22.31, 68.42]^{\mathrm{T}}$ arcsec and $[2.618\times10^{-3}, 2.6612\times10^{-3}, 2.577\times10^{-3}]^{\mathrm{T}}$ (°)/s, respectively, providing favorable initial conditions for the subsequent estimation of star position and blur kernel.

4.2 Restoration effect of a nonlinear-blurred image with different degrees

The attitude and gyro drift estimated by MEKF are used to calculate the heterogeneous blur kernel and the other two blur kernels. The calculations of the blur kernels (l,θ) proposed by Yi et al. (2023) and Ma et al. (2016) are as Eqs. (41) and (42), respectively:

$$\begin{cases} l=\sum\limits_{m=1}^{n}\sqrt{(x_i^m-x_i^{m-1})^2+(y_i^m-y_i^{m-1})^2}, \\ \theta=\dfrac{1}{n}\sum\limits_{m=1}^{n}\arctan\left(\dfrac{y_i^{t+m\delta t}-y_i^{t+(m-1)\delta t}}{x_i^{t+m\delta t}-x_i^{t+(m-1)\delta t}}\right), \end{cases} \tag{41}$$

$$\begin{cases} l=\left\lfloor\dfrac{\sqrt{\omega_x^2+\omega_y^2}T}{\theta_{\mathrm{FOV}}}N\right\rfloor, \\ \theta=\arctan\dfrac{\omega_x}{\omega_y}, \end{cases} \tag{42}$$

where (x_i^m, y_i^m) represents the position of the i^{th} star at time m of gyro sampling within the exposure time. n denotes the total number of times the gyro collects data within one exposure time of the star sensor. The compensated angular velocity is denoted by $\boldsymbol{\omega}=(\omega_x,\omega_y,\omega_z)^{\mathrm{T}}$, and T and θ_{FOV} denote the exposure time and field of view of the star sensor, respectively. N denotes the number of pixels corresponding to the field of view. $\lfloor\rfloor$ signifies the operation of rounding down to the nearest integer.

The star images with different degrees of nonlinear motion blur correspond to different proportions of the Z-axis components of the angular velocity. In this simulation, the modulus of the angular velocity is fixed at 10 (°)/s. The angle between the angular velocity vector and the Z axis is incremented from 0 to 90° with a step size of 10°. For each set of angular velocity, simulated motion-blurred star images are generated, and Gaussian noises with a mean

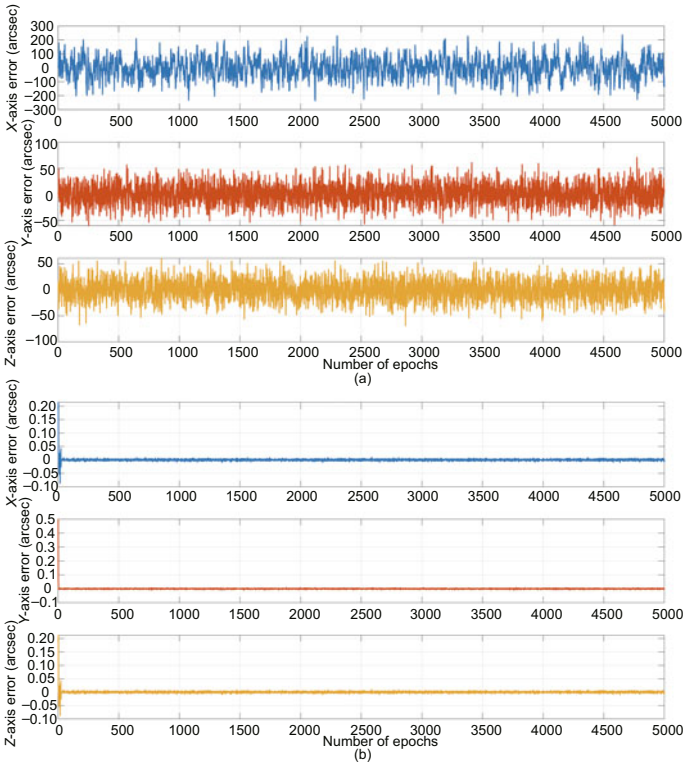

Fig. 6 Performance of the MEKF at an angular velocity of 5 (°)/s: (a) error angle; (b) error of the gyro drift. Note that 1 epoch equals 0.2 s

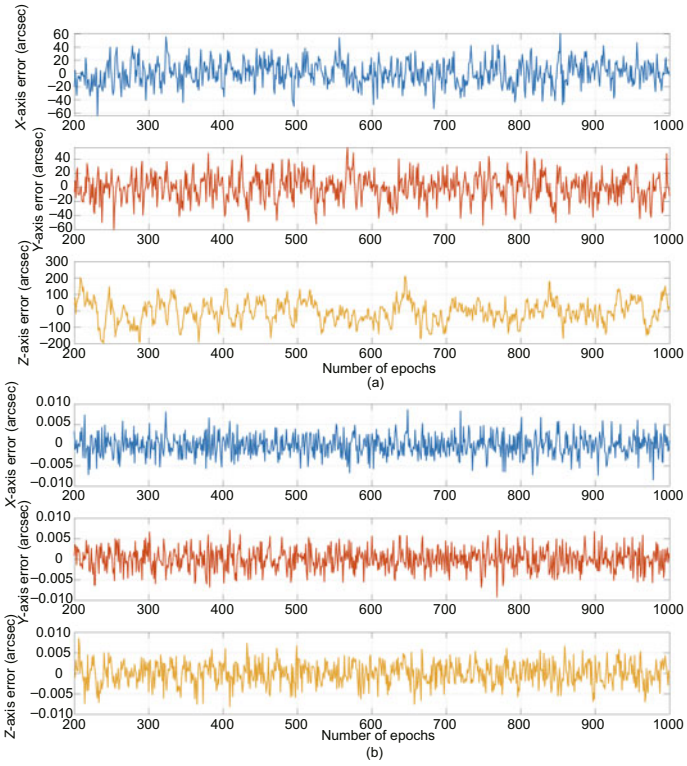

Fig. 7 Performance details of the MEKF at an angular velocity of 5 (°)/s: (a) error angle; (b) error of the gyro drift. Note that 1 epoch equals 0.2 s

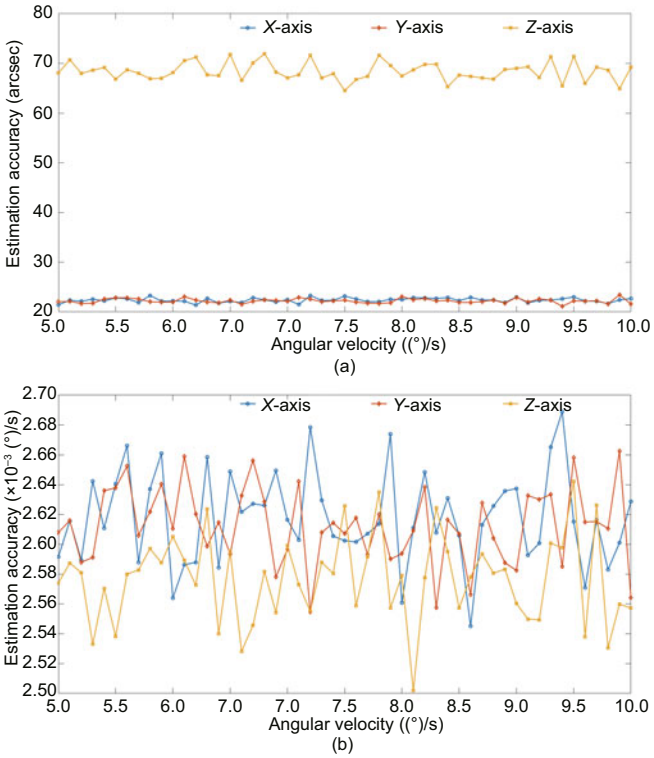

Fig. 8 Global performance of the MEKF: (a) estimation accuracy of the attitude; (b) estimation accuracy of the gyro drift

of 20 and a standard deviation σ of 5, 7, and 10 are added. Then, the three algorithms are used for image restoration and centroid extraction, and the performances of the algorithms are evaluated by the RMSE of the position error of centroid extraction.

The image restoration results of the proposed algorithm are shown in Fig. 9. It is evident that the algorithm effectively concentrates the energy of the dispersed star points.

RMSE of the position errors of three algorithms under different degrees of nonlinear motion blur and various noise conditions is shown in Figs. 10–12. When the Z-axis component of the angular velocity is relatively high, the image restoration accuracy of each algorithm is high. This is because although the angular velocity reaches 10 (°)/s, the trailing length at the edge of the image is about 7.15 pixels, while there is almost no trailing of the star spot near the center of the image. In this case, compared with the method proposed by Ma et al. (2016), which directly extracts the centroids of star spots, the other two methods have higher accuracy. As the proportion of the Z-axis component of the angular velocity decreases, the extraction accuracies of the other two

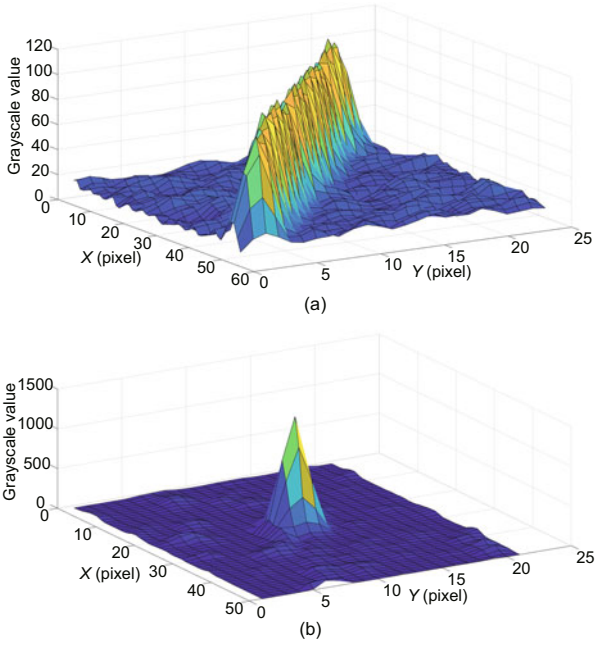

Fig. 9 Image restoration effect of the proposed algorithm: (a) motion-blurred star spot; (b) star spot recovered by the proposed algorithm

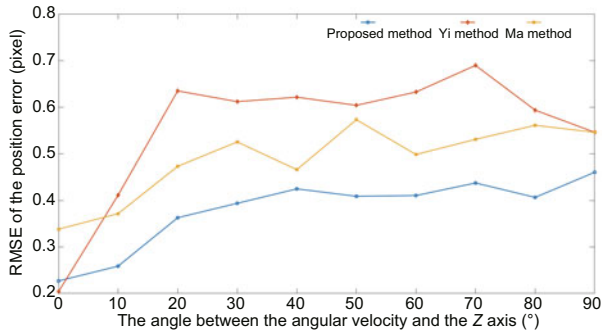

Fig. 10 RMSE of the position error when σ is 5. Yi method is from Yi et al. (2023) and Ma method is from Ma et al. (2016)

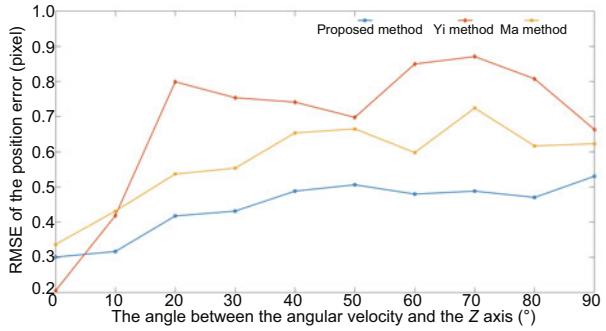

Fig. 11 RMSE of the position error when σ is 7. Yi method is from Yi et al. (2023) and Ma method is from Ma et al. (2016)

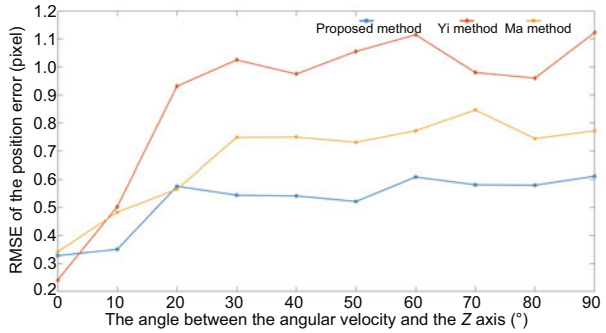

Fig. 12 RMSE of the position error when σ is 10. Yi method is from Yi et al. (2023) and Ma method is from Ma et al. (2016)

methods fluctuate greatly, while the proposed algorithm is more accurate and stable. In addition, compared with the other two methods, the proposed method demonstrates robustness to noise. With the increase of noise, even if the standard deviation σ of Gaussian noise reaches 10, the extraction accuracy can still be maintained at about 0.6 pixels.

4.3 Performance of the image restoration

To evaluate the performance of the three methods, the angular velocity is varied within the range of 5 to 10 (°)/s with a step size of 0.1 (°)/s, and the direction of the angular velocity is set to any direction. The simulated motion-blurred star images are generated based on each set of angular velocity, and Gaussian noise with a mean of 20 and a standard deviation σ of 5 is added. Furthermore, to verify the optimization effect of MEKF in removing measurement noise and gyro drift on image restoration, the heterogeneous blur kernel estimation algorithm with an uncompensated error is also used for comparison. The four methods are used for star image restoration and centroid extraction, and the performances of the methods are evaluated by the RMSE of the accuracy of centroid extraction.

As shown in Fig. 13, using the MEKF for the estimation and compensation of measurement errors from the star sensor and gyro drift leads to a significant enhancement in the accuracy of centroid extraction. In addition, since the proposed algorithm is pixel-by-pixel deblurring based on the cause of motion blur, the extraction accuracies of various motion-blurred star images are relatively stable, while the restoration effects of the other two algorithms fluctuate greatly with the change of angular velocity. The average values of the extraction accuracy and computation time are presented in Table 4. Compared with the uncompensated method, the star extraction accuracy of the proposed algorithm is improved by 48.11% after compensating for the measurement error of the star sensor and gyro drift with MEKF. Compared with the other two algorithms, the extraction accuracy of the proposed algorithm is improved by 59.64% (compared with Ma et al. (2016)'s algorithm) and 36.63% (compared with Yi et al. (2023)'s algorithm). However, the proposed algorithm takes a long time for blur kernel estimation and image restoration because the proposed

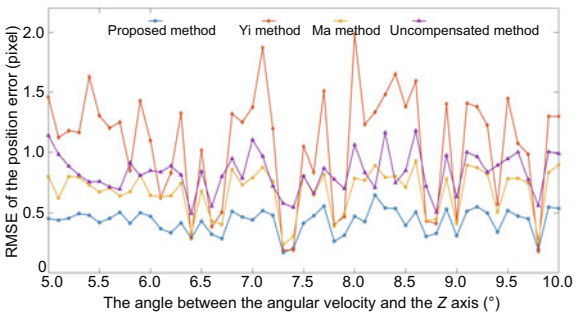

Fig. 13 RMSE of the extraction accuracy with varying angular velocities

Table 4 Performance of the algorithms

Method	Extraction accuracy (pixel)	Time of blur kernel estimation (ms)	Time of restoration (ms)
Proposed method	0.4319	1.6	97.7
Ma et al. (2016)'s method	1.0700	1.1×10^{-2}	2.4
Yi et al. (2023)'s method	0.6816	6.9×10^{-3}	104
Uncompensated method	0.8324	1.5	98.5

algorithm needs to calculate the blur kernel corresponding to each pixel in the star position. If only the star position is restored, the required time is close to the time of restoring the whole star image with a single blur kernel, which is also the limitation of the entire algorithm.

Then the star spots recovered by the proposed method are used for attitude estimation, and the accuracy of the attitude estimation is quantified as the RMSE of the three-axis error angle according to Eq. (1). The result is shown in Fig. 14.

Compared with the initial measurement noise $[30, 30, 200]^{\mathrm{T}}$ arcsec of the star sensor, the proposed algorithm has an average attitude estimation accuracy of $[3.317, 2.913, 42.13]^{\mathrm{T}}$ arcsec, the accuracy of the pointing axis is improved by 78.94%, and the accuracies of the other two axes are improved by 88.94% and 90.29%, which greatly improves the dynamic performance of the star sensor.

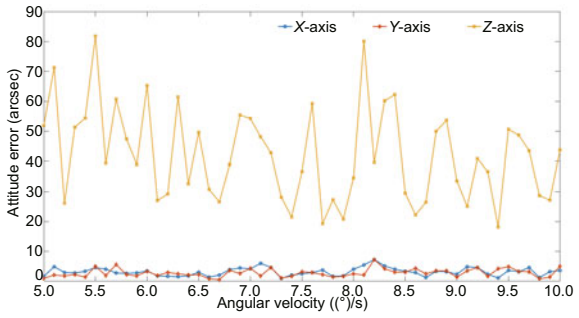

Fig. 14 Attitude estimation accuracy with varying angular velocities

5 Conclusions

The MEKF-aided non-blind star image restoration algorithm based on the heterogeneous blur kernel is proposed to address challenges in estimating gyro drift and restoring non-uniform and nonlinear motion-blurred images. The simulation results indicate that the proposed algorithm can effectively eliminate the measurement error of the star sensor and the gyro drift and improve the effect of star image restoration. After compensating for the error, the performance of the proposed algorithm is improved by 48.11%. The proposed algorithm is also robust to image noise. Even if the standard deviation σ of Gaussian noise reaches 10, the extraction accuracy after image restoration with a heterogeneous blur kernel can still be maintained at about 0.6 pixels. Compared with the existing algorithms, when the proposed algorithm is used to estimate the heterogeneous blur kernel and restore the star image, the extraction accuracy is improved by 59.64% (compared with Ma et al. (2016)'s algorithm) and 36.63% (compared with Yi et al. (2023)'s algorithm). Compared with the initial measurement noise, the accuracy of the pointing axis is improved by 78.94%, and the accuracies of the other two axes are improved by 88.94% and 90.29%. Simulation results reveal that the proposed algorithm exhibits high precision, is robust to noise, and is suitable for the restoration of various motion-blurred images.

Moreover, while the proposed algorithm demonstrates promising performance, it also presents certain limitations. First, the pixel-wise heterogeneous blur kernel estimation introduces high computational complexity, which may hinder real-time applications, especially in high-resolution scenarios. Second, the current evaluation is primarily based on the simulated star images with an idealized noise model. Due to the limited availability of the real star images under high dynamic conditions, actual star-sensitive data have not been used for validation. As a result, discrepancies between the simulated and real-world noise distributions may exist, potentially affecting the generalizability of the results. Future research will focus on reducing the algorithm's computational load—potentially via model simplification, parallel processing, or hardware acceleration—and validating the proposed method using real on-orbit data to further assess its robustness under practical conditions.

Contributors

Yang LIU, Hao WANG, and Zhonghe JIN conceived and designed the research. Yang LIU drafted the paper. Huajian DENG, Hao WANG, and Zhonghe JIN helped organize the paper. Yang LIU revised and finalized the paper.

Conflict of interest

Zhonghe JIN is an editorial board member of *Frontiers of Information Technology & Electronic Engineering*; he was not involved with the peer review process of this paper. All the authors declare that they have no conflict of interest.

Data availability

The data that support the findings of this study are available from the corresponding author upon reasonable request.

References

Bright DS, Steel EB, 1987. Two-dimensional top hat filter for extracting spots and spheres from digital images. *J Micros*, 146(2):191-200. https://doi.org/10.1111/j.1365-2818.1987.tb01340.x

Fei X, Nan C, Zheng Y, et al., 2012. A novel approach based on MEMS-Gyro's data deep coupling for determining the centroid of star spot. *Math Probl Eng*, 2012(1):403584. https://doi.org/10.1155/2012/403584

Gong D, Yang J, Liu LQ, et al., 2017. From motion blur to motion flow: a deep learning solution for removing heterogeneous motion blur. Proc IEEE Conf on Computer Vision and Pattern Recognition, p.2319-2328. https://doi.org/10.1109/CVPR.2017.405

Hou YX, Zhao RJ, Ma YB, et al., 2021. A real-time star tailing removal method based on fast blur kernel estimations. *Math Probl Eng*, 2021:8819277. https://doi.org/10.1155/2021/8819277

Jiang J, Huang JN, Zhang GJ, 2017. An accelerated motion blurred star restoration based on single image. *IEEE Sens J*, 17(5):1306-1315. https://doi.org/10.1109/JSEN.2016.2645861

Lefferts EJ, Markley FL, Shuster MD, 1982. Kalman filtering for spacecraft attitude estimation. *J Guid Contr Dyn*, 5(5):417-429. https://doi.org/10.2514/3.56190

Li AJ, Liu CS, Shen XF, 2013. An approach to star map simulation for star sensor considering the effect of image motion. *Opt Photo J*, 3(2B):108-111. https://doi.org/10.4236/opj.2013.32B027

Ma LH, Bernelli-Zazzera F, Jiang GW, et al., 2016. Region-confined restoration method for motion-blurred star image of the star sensor under dynamic conditions. *Appl Opt*, 55(17):4621-4631. https://doi.org/10.1364/AO.55.004621

Ma LH, Dai DK, Ni YM, 2025. How to improve the attitude accuracy of the star sensor under dynamic conditions: a review. *Acta Astronaut*, 233:42-54. https://doi.org/10.1016/j.actaastro.2025.03.043

Madyastha V, Ravindra V, Mallikarjunan S, et al., 2011. Extended Kalman filter vs. error state Kalman filter for aircraft attitude estimation. Proc AIAA Guidance, Navigation, and Control Conf, Article 6615. https://doi.org/10.2514/6.2011-6615

Markley FL, 2003. Attitude error representations for Kalman filtering. *J Guid Contr Dyn*, 26(2):311-317. https://doi.org/10.2514/2.5048

Sola J, 2017. Quaternion kinematics for the error-state Kalman filter. https://arxiv.org/abs/1711.02508

Spiller D, Curti F, 2022. A geometrical approach for the angular velocity determination using a star sensor. *Acta Astronaut*, 196:414-431. https://doi.org/10.1016/j.actaastro.2020.11.043

Sun T, Xing F, You Z, et al., 2013. Motion-blurred star acquisition method of the star tracker under high dynamic conditions. *Opt Expr*, 21(17):20096-20110. https://doi.org/10.1364/OE.21.020096

Sun T, Xing F, You Z, et al., 2014a. Deep coupling of star tracker and MEMS-Gyro data under highly dynamic and long exposure conditions. *Meas Sci Technol*, 25(8):085003. https://doi.org/10.1088/0957-0233/25/8/085003

Sun T, Xing F, You Z, et al., 2014b. Smearing model and restoration of star image under conditions of variable angular velocity and long exposure time. *Opt Expr*, 22(5):6009-6024. https://doi.org/10.1364/OE.22.006009

Tian CG, Hao N, He FH, 2025. T-ESKF: transformed error-state Kalman filter for consistent visual-inertial navigation. *IEEE Robot Autom Lett*, 10(2):1808-1815. https://doi.org/10.1109/LRA.2024.3524905

Wang H, Wang ZY, Wang BD, et al., 2020. An artificial intelligence enhanced star identification algorithm. *Front Inform Technol Electron Eng*, 21(11):1661-1670. https://doi.org/10.1631/FITEE.1900590

Wang KD, Zhang C, Li Y, et al., 2014. A new restoration algorithm for the smeared image of a SINS-aided star sensor. *J Navig*, 67(5):881-898. https://doi.org/10.1017/S0373463314000277

Wang SQ, Zhang SJ, Ning MF, et al., 2018. Motion blurred star image restoration based on MEMS gyroscope aid and blur kernel correction. *Sensors*, 18(8):2662. https://doi.org/10.3390/s18082662

Yang L, Huajian D, Yuchen L, et al., 2025. Motion parameters estimation algorithm of star sensor based on Zernike moments under dynamic conditions. *Meas Sci Technol*, 36(5):055104. https://doi.org/10.1088/1361-6501/adc1ec

Yi JH, Ma YB, Zhu ZF, et al., 2023. A blurred star image restoration method based on gyroscope data and enhanced sparse model. *Meas Sci Technol*, 34(11):115105. https://doi.org/10.1088/1361-6501/ace730

Zamani M, Trumpf J, Mahony R, 2015. Nonlinear attitude filtering: a comparison study. https://arxiv.org/abs/1502.03990

Zhang WN, Quan W, Guo L, 2012. Blurred star image processing for star sensors under dynamic conditions. *Sensors*, 12(5):6712-6726. https://doi.org/10.3390/s120506712